Accepted Manuscript

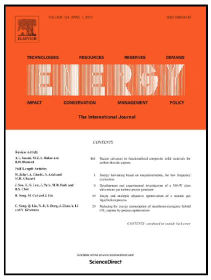

Darrieus Wind Turbine Blade Unsteady Aerodynamics: a Three-Dimensional Navier-Stokes CFD assessment

Francesco Balduzzi, Jernej Drofelnik, Alessandro Bianchini, Giovanni Ferrara, Lorenzo Ferrari, Michele Sergio Campobasso

PII: S0360-5442(17)30582-0

DOI: 10.1016/j.energy.2017.04.017

Reference: EGY 10655

To appear in: *Energy*

Received Date: 28 September 2016

Revised Date: 07 March 2017

Accepted Date: 04 April 2017

- Analysis of the 3D unsteady aerodynamics of a Darrieus wind turbine blade in motion
- Highly spatially and temporally refined time-dependent simulations carried out with the COSA code
- One month calculation time on more than 16.000 processors on a IBM BG/Q cluster
- Detailed description of: tip losses, dynamic stall, vortex propagation and blade/wake interaction

Darrieus Wind Turbine Blade Unsteady Aerodynamics: a Three-Dimensional Navier-Stokes CFD assessment

Francesco Balduzzi[1], Jernej Drofelnik[2], Alessandro Bianchini[1], Giovanni Ferrara[1], Lorenzo Ferrari[3*], Michele Sergio Campobasso[4]

[1] Department of Industrial Engineering, University of Florence - Via di Santa Marta 3, 50139, Firenze, Italy - Tel. +39 055 275 8773 - Fax +39 055 275 8755 - balduzzi@vega.de.unifi.it

[2] School of Engineering, University of Glasgow - James Watt Building South, University Avenue, G12 8QQ Glasgow, UK - Tel. +44 (0)141 330 2032 - j.drofelnik.1@research.gla.ac.uk

[3] Department of Energy, Systems, Territory and Construction Engineering, University of Pisa - Largo Lucio Lazzarino, 56122, Pisa, Italy - Tel. +39 050 221 7132 - Fax +39 050 221 7333 - lorenzo.ferrari@unipi.it*

[4] Department of Engineering, Lancaster University - Gillow Avenue - LA1 4YW Lancaster, UK - Tel. +44 (0)1524 594673 - Fax +44 (0)1524 381707 - m.s.campobasso@lancaster.ac.uk

[*] = contact author

Abstract

Energized by the recent rapid progress in high-performance computing and the growing availability of large computational resources, computational fluid dynamics (CFD) is offering a cost-effective, versatile and accurate means to improve the understanding of the unsteady aerodynamics of Darrieus wind turbines, increase their efficiency and delivering more cost-effective and structurally sound designs.

In this study, a Navier-Stokes CFD research code featuring a very high parallel efficiency was used to thoroughly investigate the three-dimensional unsteady aerodynamics of a Darrieus rotor blade. Highly spatially and temporally resolved unsteady simulations were carried out using more than 16,000 processor cores on an IBM BG/Q cluster. The study aims at providing a detailed description and quantification of the main three-dimensional effects associated with the periodic motion of this turbine type, including tip losses, dynamic stall, vortex propagation and blade/wake interaction. Presented results reveal that the three-dimensional flow effects affecting Darrieus rotor blades are significantly more complex than assumed by the lower-fidelity models often used for design applications, and strongly vary during the rotor revolution. A comparison of the CFD integral estimates and the results of a blade-element momentum code is also presented to highlight strengths and weaknesses of low-fidelity codes for Darrieus turbine design.

The reported CFD results provide a valuable and reliable benchmark for the calibration of lower-fidelity models, which are still key to industrial design due to their very high execution speed.

Keywords

Darrieus wind turbine, unsteady Navier-Stokes simulations, CFD, tip flows

Nomenclature

Latin symbols		
AoA	angle of attack	
AR	aspect ratio	[-]
c	blade chord	[m]
C_t	torque coefficient	[-]
C_p	pressure coefficient	[-]
CP	power coefficient	[-]
BEM	Blade Element Momentum	
CFD	Computational Fluid Dynamics	
H	turbine height	[m]
k	turbulent kinetic energy	[m^2/s^2]
NS	Navier-Stokes	
p	static pressure	[Pa]
PDEs	Partial Differential Equations	
R	turbine radius	[m]
RANS	Reynolds-Averaged Navier-Stokes	
SST	Shear Stress Transport	
T	torque per unit length	[Nm]
TSR	tip-speed ratio	[-]
u, v, w	Cartesian components of local fluid velocity vector	[m/s]
U	magnitude of absolute wind speed	[m/s]
$\underline{v}$	local fluid velocity vector	[m/s]
$\underline{v}_b$	local grid velocity vector	[m/s]
VAWTs	Vertical-Axis Wind Turbines	
W	magnitude of relative wind speed	[m/s]
x, y, z	reference axes	
y^+	dimensionless wall distance	[-]
Greek symbols		
ϑ	azimuthal angle	[deg]
μ_t	turbulent viscosity	[Kg/m/s]
ρ	air density	[kg/Nm^3]
Φ	computational domain diameter	[m]
Ψ	computational domain height	[m]
ω	specific turbulence dissipation rate	[1/s]
Ω	turbine revolution speed	[rad/s]
Subscripts		
∞	value at infinity	
ave	averaged value	

1. Introduction

1.1 Background

After most research on vertical-axis wind turbines (VAWTs) came to a standstill in the mid 90's [1], the Darrieus wind turbine [2] is receiving again increasing attention of both researchers and manufacturers [3-6]. For distributed wind power generation in the built environment [7], inherent advantages of this turbine type, such as performance insensitivity to wind direction, generator often positioned on the ground, low noise emissions [8], enhanced performance in skewed [9] or highly turbulent and unsteady flows [10-12], may outweigh disadvantages, such as lower power coefficients and more difficult start-up, with respect to typical horizontal axis machines. Moreover, in densely populated areas VAWTs are often preferred to other turbine types because they are perceived as aesthetically more pleasant and thus easier to integrate in the landscape [13]. The applicability of Darrieus wind turbines for utility-scale power generation making use of floating platforms also appears to present important benefits in terms of overall dynamic stability [14].

Historically, the aerodynamic performance analysis of these rotors has been carried out with low-fidelity methods, like the Blade Element Momentum (BEM) theory [1,15-17] or lifting line methods [18-19]. More recently, however, the intrinsic limitations of these models made clear that higher-fidelity tools are needed in order to understand in greater depth the complex unsteady aerodynamics of Darrieus rotors [20], such as the interaction of the blades with macro vortices [21] or dynamic stall [22].

While experimental testing is often quite difficult and expensive, Navier-Stokes (NS) Computational Fluid Dynamics (CFD) can be a versatile and accurate means to improve the understanding of VAWT unsteady aerodynamics and achieve higher-performance, structurally sound and more cost-effective Darrius turbine designs. The use of NS CFD for simulating time-dependent Darrieus turbine aerodynamics is rapidly increasing due to both the ongoing development and deployment of more powerful high-performance computing hardware, such as large clusters of multi- and many-core processors [23], and also the development of computationally more efficient algorithms.

1.2 Previous CFD studies on Darrieus VAWTs

Early use of the Reynolds-Averaged Navier-Stokes (RANS) CFD technology for Darrieus rotor aerodynamics for investigating the complex fluid mechanics of these machines was based mostly on two-dimensional (2D) simulations (e.g. [24]). An extensive literature review of 2D RANS CFD studies is provided by Balduzzi et al. [25], along with an overview of the numerical settings frequently used for Darrieus rotor RANS studies and guidelines for the optimal set-up of these simulations. Two-dimensional RANS analyses, suitably corrected for three-dimensional (3D) effects, such as struts resistive torque and blade tip losses, have been used to estimate the turbine overall performance [26] and predominantly 2D phenomena, like virtual camber [27] and virtual incidence [28] effects, the influence of unsteady wind conditions on turbine aerodynamics [29], the evolution of the flow field at start-up [30], and turbine/wake interactions [31].

However, the use of 2D simulations to analyse the flow field past real rotors may result in significant uncertainties, due to the difficulty of reliably quantifying complex 3D aerodynamic features such as blade tip flows, their dependence on the blade tip geometry and their impact on the overall efficiency as a function of the blade aspect ratio. Moreover, most 3D aerodynamic features of Darrieus rotor flows vary not only spatially (e.g. dynamic stall decreases from midspan to the blade tips, as shown below), but also temporally during each revolution. It is difficult to develop corrections to improve the predictions of time-dependent 2D CFD analyses, and the resulting uncertainty on unsteady loads may severely impair both aerodynamic and structural (e.g. fatigue) assessments. Therefore 3D CFD simulations are key to characterizing and quantifying the aforementioned 3D aerodynamic phenomena. This is important for reducing the uncertainty associated with modeling such phenomena on the basis of a relatively small amount of data referring to existing turbines, and assumptions based on overly simplistic analytical models. However, large computational resources are needed for such simulations, due to the high temporal and spatial grid refinement needed for accurately resolving all design-driving aerodynamic phenomena.

Comparisons of 2D and 3D simulations are sometimes carried out considering test cases for which experimental data are available, as in Howell et al. [32] and Lam et al. [33]. In [32] the use of 2D RANS CFD led to relatively poor agreement with experiments: a maximum power coefficient *CP* of 0.371 at a tip-speed ratio (TSR) of 2.4 was predicted against a measured maximum *CP* of 0.186 at TSR=1.85. Using 3D simulations, the maximum power coefficient was instead correctly predicted, although the shape of computed and measured power curves presented significant differences. The k-ε re-normalization group turbulence model [34] was used for all simulations, but no detailed information on the mesh size was provided, except for the indication of a high dimensionless wall distance ($y^+ \approx 10$) which required the use of wall functions. Also in [35] notable discrepancies between the results of 2D and 3D RANS simulations were observed: the 2D simulations predicted a maximum power coefficient of 0.43 at TSR=4.5 against a maximum *CP* of 0.27 at TSR=1.85 predicted by the 3D analyses. A fairly coarse grid, consisting of 2.95 million elements was used for the 3D simulations of the considered two-blade rotor, and the k-ω Shear Stress Transport (SST) turbulence model [36] was used.

Gosselin et al. [37] used 2D and 3D RANS simulations with the k-ω SST turbulence model to investigate the dependence of 3D effects on the blade aspect ratio, finding that an aspect ratio of 7 led to a relative efficiency drop of 60 percent with respect to the 2D analysis. Although the simulations were performed with very refined meshes (up to 700 nodes on each airfoil), the article reports that no rigorous mesh-independence was obtained. Joo et al. [38] analysed the aerodynamic characteristics of a two-blade rotor as a function of design parameters such as solidity and optimal TSR using the 3D RANS model coupled to a realizable k-ε turbulence model. They used a computational mesh of 1.2 million elements and compared their baseline results with available experimental data: a general overestimation of the power curve was noticed, with a 10% discrepancy at the peak power. Moreover, significant shape differences of computed and measured power curves were observed, particularly in the right branch of such curves (i.e. for high TSR values), with the measured curve being steeper than the computed one. A two-blade Darrieus rotor with straight blades was analysed by Li et al. [35,39] by means of wind tunnel experiments and 3D RANS simulations using the k-ω SST turbulence model. Numerical results compared favourably to experimental data in the left branch (i.e. low TSR values) of the power curve, but CFD significantly overestimated power for higher TSR, possibly due to excessively small distance between the rotor and the farfield boundaries of the physical domain (about 2 rotor diameters from the rotor center). The simulations used a grid with about 5 million elements, and predicted a peak power coefficient of 0.24 at TSR=2.09 whereas experiments showed a peak *CP* of 0.18 at TSR=2.18.

Alaimo et al. [40] carried out a comparative study of the aerodynamic performance of three-blade Darrieus rotors using straight and helical blades. For the three-blade rotors they analysed, they found that blade tip vortex flows significantly reduced the rotor performance and that the use of helical blades significantly reduces this power loss. The largest grids used for those 3D RANS analyses had about 10 million elements, and turbulence was modelled using the k-ε turbulence model with wall functions to enable the use of relatively coarse grids and enhance numerical stability. De Marco et al. [41] performed 3D RANS simulations to analyse the influence of the geometry of the blade supporting arms on the turbine performance. Using grids featuring between 4 and 18 million elements and the k-ω SST model, they found that inclined and aerodynamically shaped supporting arms can significantly increase the mean power coefficient. Using computational meshes with up to 12 million elements and the k-ω SST model, Zamani et al. [42] characterized with 3D RANS simulations the impact of J-shaped blades on Darrieus rotor torque and power characteristics at low and medium TSR values, finding that this blade shape significantly increases the rotor performance in these regimes, resulting in improved start-up characteristics. Orlandi et al. [43] used 3D RANS simulations and the k-ω SST model to study the influence of skewed wind conditions on the aerodynamic characteristics of a two-blade Darrieus turbine; to limit the computational burden of the 3D analyses, grids with about 10 million elements were used.

A recent Navier-Stokes CFD study of a three-blade Darrieus rotor using pitching blades to further improve the aerodynamic performance has made use of a Large Eddy Simulation [44], an approach that can yield more accurate results than the RANS method. However, resolved LES analyses require computational grids far larger than those needed for grid-independent RANS analyses, and this makes the use of resolved 3D LES simulations even more difficult than that of grid-independent 3D RANS analyses.

The aforementioned 3D CFD analyses highlighted new important aerodynamic phenomena, but in almost all cases limited availability of computational resources imposed the use of fairly coarse spatial and temporal refinement, and this may result in uncertainty due to lack of complete grid-independence of the CFD solutions. Recent parametric analyses investigating the impact of several numerical parameters on the computationally less demanding 2D CFD analysis of Darrieus rotors [25,45-47] showed that the analysis reliability - in terms of accuracy of both performance prediction and resolution of important flow structures - is tremendously affected by the quality of the meshing and time-stepping strategies. These studies highlighted that the minimum temporal and spatial refinement required to obtain grid-independent solutions is quite high, due to the aerodynamic complexity of these unsteady flows. Because of these constraints, the computational cost of reliable 3D unsteady NS analyses of Darrieus rotor flows is extremely large due to the necessity of maintaining the high temporal resolution indicated by the 2D parametric studies and a high level of spatial refinement both in the grid planes normal to the rotor axis and the 3rd direction orthogonal to such planes. Refinement in the 3rd direction is essential to reliably resolving 3D flow features. For example, the parametric study of [25] showed that temporal and spatial grid-independent 2D RANS analyses of a three-blade rotor require grids with at least 400,000 elements. To preserve the same accuracy level in a 3D RANS simulation of the same turbine (modelling only half of the rotor making use of symmetry boundary conditions on the plane at rotor midspan and ensuring adequate refinement in the tip region) the mesh would consist of at least 90 million elements, which is almost ten times the size of the finest meshes used in the 3D RANS studies of Darrieus rotor flows published to date. Failing to maintain these refinement levels may reduce the benefits achievable by using 3D RANS simulations to improve Darrieus rotor design.

1.3 Study aim

In this study, the COSA RANS research code, which features a very high parallel efficiency, is used to investigate in great detail the 3D flow features of a rotating Darrieus rotor blade and the impact of flow three-dimensionality on power generation efficiency. More specifically, the study aims at providing a highly accurate analysis of the main 3D phenomena occurring during each revolution of the considered one-blade rotor, including tip vortices, dynamic stall and downstream vortex propagation, and to assess the impact of these phenomena on the overall performance of this rotor. The use of a single rotating blade for the type of analyses reported herein is not uncommon (see for example [40]). This set-up enables a better understanding of individual key fluid mechanics phenomena adversely impacting loads and energy efficiency of Darrieus rotors, and this information constitutes the first knowledge level required to improve the design of these machines. Follow-on studies will focus on additional 3D fluid mechanic aspects resulting from the multi-blade environment making use of computational resources larger than those used in the present study.

To maximize the analysis reliability, a time-dependent 3D simulation using very high levels of spatial and temporal refinement is carried out using a large 98,304-core IBM BG/Q cluster.

The presented test case is expected to be highly valuable to other research groups both to verify new CFD approaches and to calibrate lower-fidelity models (e.g. model based on lifting line theory and free vortex methods), which are key to industrial design due to their extremely low computational cost.

The paper is organized as follows. Section 2 presents the numerical methodology that has been followed in the study: sub-section 2.1 reports the governing equations solved by the COSA CFD code for the analysis of Darrieus rotor flows, sub-section 2.2 summarizes the main numerical features and previous work carried out with this code, and sub-section 2.3 provides the main features of the case study and describes the adopted numerical set-up. Section 3 presents the main results of the 3D CFD analysis and compares them to those of the 2D analysis of the same case study, to highlight the impact of 3D effects. In Section 3 the results of the RANS CFD analyses are also compared with those of the blade element momentum theory to highlight strengths and weaknesses of this engineering approach. A summary of the study and concluding remarks are finally provided in Section 4.

2. Numerical methodology

2.1 Governing equations

The compressible NS equations are a system of 5 nonlinear partial differential equations (PDEs) expressing the conservation of mass, momentum and energy in a viscous fluid flow. Averaging these equations on the longest time-scales of turbulence yields the so-called RANS equations, which feature additional terms depending on the Reynolds stress tensor. Making use of Boussinesq approximation, this tensor has an expression similar to that of the laminar or molecular stress tensor, with the molecular viscosity replaced by a turbulent or eddy viscosity [48-49]. In the COSA CFD code, the eddy viscosity is computed by means of the two-equation *k-ω* SST turbulence model [36]. Thus, turbulent flows are determined by solving a system of 7 PDEs.

Given a moving time-dependent control volume *C(t)* with time-dependent boundary *S(t)*, the Arbitrary Lagrangian–Eulerian integral form of the system of the time-dependent RANS and SST equations in an absolute frame of reference is:

$$\frac{\partial}{\partial t}\left(\int_{C(t)} \mathbf{U} dC\right) + \oint_{S(t)} \left(\underline{\Phi}_c - \underline{\Phi}_d\right) \cdot d\underline{S} - \int_{C(t)} \mathbf{S} dC = 0 \tag{1}$$

where **U** is the array of conservative variables defined as:

$$\mathbf{U} = \left[\rho \;\; \rho\underline{v}' \;\; \rho E \;\; \rho k \;\; \rho\omega\right]' \tag{2}$$

The symbols ρ, $\underline{v}$, E, k and ω denote respectively fluid density, flow velocity vector of Cartesian components (u,v,w), total energy per unit mass, turbulent kinetic energy per unit mass and specific dissipation rate of turbulent energy, and the superscript $'$ denotes the transpose operator. The total energy is defined as $E=e+(\underline{v}\cdot\underline{v})/2+k$, where e denotes the internal energy per unit mass; the perfect gas law is used to express the static pressure p as a function of ρ, E, k and the mean flow kinetic energy per unit mass $(\underline{v}\cdot\underline{v})/2$. The generalized convective flux vector is defined as:

$$\underline{\mathbf{\Phi}}_c = \mathbf{E}_c \underline{i} + \mathbf{F}_c \underline{j} + \mathbf{G}_c \underline{k} - \underline{v}_b \mathbf{U} \tag{3}$$

where $\mathbf{E}_c$, $\mathbf{F}_c$ and $\mathbf{G}_c$ are respectively the x-, y- and z-component of $\underline{\mathbf{\Phi}}_c$ and are given by:

$$\begin{cases} \mathbf{E}_c = \left[\rho u \;\; \rho u^2 + p \;\; \rho uv \;\; \rho uw \;\; \rho uH \;\; \rho uk \;\; \rho u\omega\right]' \\ \mathbf{F}_c = \left[\rho v \;\; \rho uv \;\; \rho v^2 + p \;\; \rho vw \;\; \rho vH \;\; \rho vk \;\; \rho v\omega\right]' \\ \mathbf{G}_c = \left[\rho w \;\; \rho uw \;\; \rho vw \;\; \rho w^2 + p \;\; \rho wH \;\; \rho wk \;\; \rho w\omega\right]' \end{cases} \quad (4)$$

in which $H=E+p/\rho$ is the total enthalpy per unit mass. The vector $\underline{v}_b$ is the velocity of the boundary S, and the flux term $-\underline{v}_b\mathbf{U}$ is its contribution of the boundary motion to the overall flux balance.

The expressions of the diffusive fluxes $\underline{\mathbf{\Phi}}_c$ and the turbulent source term $\boldsymbol{S}$ appearing in Eq. (1) can be found in [48] and [50].

2.2 COSA CFD code

COSA is a compressible density-based finite volume code that solves the system of PDEs corresponding to Eq. (1) using structured multi-block grids. The code features a steady flow solver, a time-domain (TD) solver for the solution of general unsteady problems [48-49], and a harmonic balance solver for the rapid solution of periodic flows [50-52]. The second-order space discretization of the convective fluxes of both the RANS and the SST equations uses an upwind scheme based on Van Leer's MUSCL extrapolations and Roe's flux difference splitting. The second order discretization of all diffusive fluxes is instead based on central finite-differencing. The space-discretized RANS and SST equations are integrated in a fully-coupled fashion with an explicit solution strategy based on full approximation scheme multigrid featuring a four-stage Runge-Kutta smoother. Convergence acceleration is achieved by means of local time-stepping and implicit residual smoothing. For general time-dependent problems, the TD equations are integrated using a second order accurate dual time-stepping approach.

Comprehensive information on the numerical methods used by COSA and thorough validation analyses are reported in [50,52] and other references cited therein. For unsteady problems involving oscillating wings and cross-flow open rotors such as the Darrieus turbines, COSA solves the governing equations in the absolute frame of reference using body-fitted grids. In the case of Darrieus rotors in open field operation this implies that the entire computational grid rotates about the rotational axis of the turbine. The suitability of COSA for the simulation of Darrieus wind turbines has been recently assessed through comparative analyses with both commercial CFD codes and experimental data [53-54].

2.3 Case study and computational model

The selected case study is a one-blade H-Darrieus rotor using the NACA 0021 airfoil. The blade chord (c=0.0858 m), the blade length (H=1.5 m) and the rotor radius (R=0.515 m) were set equal to those used in the case-study of [24]; the blade was attached to the spoke at midchord according to the original 3-blade model of [24]. The decision of simulating a single blade was based both on physical considerations and on hardware limitations. First, a one-blade model is sufficient to investigate all the desired 3D flow structures that lead to an efficiency reduction of a finite blade. At the same time, the use of a single blade allows one to isolate and analyze fundamental aerodynamic phenomena of finite-length blade aerodynamics, removing additional aerodynamic effects due to multiple blade/wake interactions occurring in a multi-blade rotor. From a practical viewpoint, the need of ensuring an adequate level of spatial refinement both in the grid planes normal to the rotor axis and in the axial direction would have required a grid with more than 100 million elements for a three-blade rotor, which was beyond the resources available for this project.

To further reduce the computational cost of the 3D simulation, the central symmetry of H-Darrieus rotors was exploited, enabling to simulate only one half of the rotor flow, thus halving computational costs. Consequently, the aspect ratio (AR) of the simulated blade portion is 8.74 which is half that of the actual blade. The modeled blade portion was contained in a cylindrical domain (Fig. 1) of radius Φ=240R, a value chosen to guarantee a full development of the wake, based on the sensitivity analyses reported in [53]. The domain height was set to Ψ=2.53H, corresponding to half the height of the wind tunnel where the original 3-blade model was tested [24,54]; measured data from these tests were previously used for validating the robustness of the RANS CFD methodology [26,53] also used in the present study.

The 3D structured multi-block grid (2D and 3D views are reported in Fig. 2) was obtained with the software ANSYS® ICEM® by first generating a 2D mesh past the airfoil using the optimal mesh settings identified in [47,49], and then extruding this mesh in the spanwise (z) direction and filling up with grid cells the volume between the blade tip and the upper (circular) farfield boundary. The far-field boundary condition enforced on the lateral (cylindrical) boundary and the upper boundary of the domain is based on suitable combinations of one-dimensional Riemann invariants and user-given freestream data, namely pressure, density and velocity components. The sub-set of these far-field data combined with suitable Riemann invariants depends on whether the fluid stream enters or leaves the computational domain at the considered boundary point (the code detects automatically inflow and outflow points of the boundaries at each iteration). The complete definition of this far-field boundary condition is provided in [55]. On the blade surface, a no-slip condition is enforced. Since the equations are solved in the absolute frame of reference, this requires imposing that the fluid velocity at the blade surface equals the velocity of the blade surface itself at the considered wall point, where pressure and density are extrapolated from the interior domain. The 2D grid section normal to the z-axis and containing the airfoil (Fig. 2(a)) consisted of 4.3×10^5 quadrilateral cells. The airfoil was discretized with 580 nodes and the first element height was set to $5.8\times10^{-5}c$ to guarantee a dimensionless wall distance y^+ lower than 1 throughout the revolution. As recommended in [25], a fairly high mesh refinement of both leading and trailing edge regions was adopted (Fig. 2(b)), and a high refinement in the airfoil region within one chord from the airfoil surface was also used to resolve the separated flow regions at high angle of attack (AoA) [27]. After extrusion in the z direction, 80 grid layers in the half-blade span were formed (Fig. 2(c)), with progressive grid clustering from midspan to tip to ensure an accurate description of tip flows. A fairly high grid refinement was also adopted in the whole tip region above the blade in order to capture the flow separation and the tip vortices. The final mesh consisted of 64 million hexahedral cells.

The rotor flow field was computed by solving the system of governing equations corresponding to Eq. (1), that is by solving the RANS and SST equations in the absolute frame of reference. In such frame, the entire body-fitted grid rotates past the rotor axis, the additional flux components due to the grid motion is accounted for by the term $-\underline{v}_b\mathbf{U}$ appearing in Eq. (3), and no sliding surface is required.

To keep computational costs within the limits of the available resources, only one operating condition was simulated, corresponding to a tip-speed ration (*TSR)* of 3.3. This condition corresponds to the same revolution speed already analyzed by some of the authors for the 3-blade turbine in [53]. For a 1-blade rotor, this TSR corresponds to a different point of the rotor power curve. The operating condition corresponding to this TSR, however, was considered of particular interest also for the 1-blade rotor because, also in this case, a) it corresponds to fairly high efficiency and thus a regime at which the rotor is expected to work more often than at other TSRs, and b) it features several complex aerodynamic phenomena (e.g. stall and strong tip vortices) posing a significant modelling challenge for the CFD analysis. Figure 3 displays the power coefficient at *TSR*=3.3 evaluated with the CFD analysis reported below on the expected power curve, which was calculated with a computationally more affordable code based on Lifting Line Theory coupled to a free vortex wake model. The model was successfully tuned on this case-study in [56] and thus it is expected to provide a power curve prediction fairly consistent with the CFD analysis reported below.

The free-stream wind speed was U=9.0 m/s. The turbulence farfield boundary conditions were a turbulent kinetic energy (k) based on 5% turbulence intensity and a characteristic length of 0.07 m.

The 3D and 2D simulations reported below were performed with the time-domain solver of COSA. The 3D simulation was run on an IBM BG/Q cluster [57] featuring 8,144 16-core nodes for a total of 98,304 cores. Exploiting the outstanding parallel efficiency of COSA, the simulation could be carried out using about 16,000 cores. This required partitioning the grid into 16384 blocks using in-house utilities, and this operation was performed starting from a grid with fewer blocks generated with the ANSYS® ICEM® grid generator. All grid blocks had identical number of cells to optimize the load balance of the parallel simulation. Using a time-discretization yielding 720 steps per revolution, the simulation needed 12 revolutions to achieve a fully periodic state. The flow field was considered periodic once the difference between the mean torque values of the last two revolutions was smaller than 0.1% of the mean torque in the revolution before the last. The wall-clock time required for this 3D simulation was about 653 hours (27.2 days).

2.4 Grid and time-step sensitivity analyses

One of the key elements of this study is that the 3D calculation was carried out using a high level of spatial and temporal resolution. The 3D grid used to carry out the analyses reported in Section 3 was obtained by extruding in the third direction the $4.3\text{x}10^5$-element 2D grid described above, and such grid was shown to provide accurate and grid-independent results in [53].

To assess the impact of using coarser spatial and temporal refinement on the computed solution, the considered flow regime was also simulated using only 360 steps per revolution and a coarser 3D grid with 8 million elements, obtained from the 64million element fine grid by removing every second line in all three directions.

The periodic profiles of the instantaneous torque coefficient C_t obtained with the coarse and fine grids are compared in Fig. 4, and the definition of C_t is provided by Eq. (5), in which T denotes the instantaneous torque on the entire blade, U_∞ and ρ_∞ denote respectively the far-field wind speed and the air density, c is the blade chord, and H is the overall blade length. The angular position ϑ=0° corresponds to the blade leading edge facing the oncoming wind and entering the upwind half of its revolution.

$$C_t = \frac{T}{\frac{1}{2}\rho_\infty U_\infty{}^2 c^2 H} \qquad (5)$$

The comparison shows that differences between the two predictions occur over most parts of the period, particularly around the maximum values of C_t. These discrepancies are caused by differences in the prediction of strength and timing of stall on the airfoils and under-resolved wakes and wake/blade interactions when using the coarse grid. The position of the curve peak (maximum C_t in the upwind region of rotor trajectory) predicted by the coarse grid has an error of about 3 degrees in azimuthal coordinates, leading to a shift of the curve in the range between ϑ=90° and ϑ=300°. Such discrepancies, reported in Fig. 4 also as the difference between the coarse and fine grid profiles normalized by the revolution-averaged mean torque of the fine grid (curve labeled "% variation") result in the mean torque coefficient obtained with the coarse grid being 3.2 percent higher than that obtained with the fine grid. As discussed in the following, this difference corresponds to nearly 40 percent of the energy efficiency loss due to finite blade length effects. This highlights the importance of using a fine grid for this type of analyses.

The impact of the mesh refinement on the resolution of some of the 3D flow phenomena occurring during the revolution are examined in Fig. 5. This figure shows the extent of the vortices generated at the blade tip at ϑ=80° predicted with the two meshes. The red and blue vortices represent the regions of ascending and descending flow, respectively. The higher dissipation of the coarse mesh leads to an under-prediction of the downstream propagation of the vortex, which is reduced from about three chords (Fig 5(b)) to less than two chords (Fig 5(a)). The coarse grid under-estimation of the tip effects contributes to the overestimation of the torque highlighted in Fig. 4. The vorticity contours at midspan when the blade is at ϑ=315° are compared in Fig. 6 to assess the resolution of the free convection of vorticity in the downstream region. With the finer mesh the wake is resolved more sharply, thus fulfilling essential prerequisites for adequately resolving blade-wake interactions in the downwind part of the revolution. The under-resolution of the wake in the downwind rotor region contributes to the higher torque produced by the blade when interacting with the wake shed in the upstream trajectory. The impact of all these vortical phenomena on the rotor performance is even higher in multi-blade rotors, due to higher number of interactions (and thus energy loss events) per revolution.

3. Results and discussion

Figure 7(a) reports the instantaneous torque coefficient per unit length (C_{tz}) at different span lengths along the blade (0 percent and 100 percent correspond to midspan and tip, respectively). The instantaneous torque coefficient per unit length C_{tz} is defined by Eq. (6). Here T_z denotes the instantaneous torque per unit blade length at the considered spanwise position.

$$C_{tz} = \frac{T_z}{\frac{1}{2}\rho_\infty {U_\infty}^2 c^2} \tag{6}$$

Figure 7(b) reports three torque profiles. The profile labelled *2D* refers to the results of a 2D simulation of the same rotor, and corresponds to the "ideal" torque of a blade with infinite span, i.e. without any secondary effects at the blade tip. This 2D simulation was carried out using a mesh equal to the midspan section of the 3D fine mesh and the same numerical parameters of the 3D simulations. The torque profile labelled "*0%"* is the torque per unit blade length at midspan of the finite-length rotor, whereas the torque profile labelled *3D* is the overall torque coefficient C_t of the 3D rotor defined in Eq. (7). The result obtained by using this definition is identical to that obtained by using Eq. (5).

$$C_t = \frac{2}{H}\int_0^{\frac{H}{2}} C_{tz}\,dz \tag{7}$$

Examination of these profiles reveals several important facts. Firstly, the ideal 2D torque and the 3D torque profiles are characterized by similar patterns, including the occurrence of two relative maxima, one in the upwind the other in the downwind regions, and also similar azimuthal positions of both maxima: the maximum torque in the upwind portion of the revolution is located at $\vartheta \approx 88.5°$ and the maximum torque in the downwind portion of the revolution is located at $\vartheta \approx 257°$ in both cases. This behaviour is in line with the analyses of both Lam [33] and Alaimo [40], which showed that the periodic torque profiles obtained with 2D and 3D simulations differ significantly for their amplitudes but have comparable shapes. Figure 7(b) also highlights that the differences between the 2D torque profile and that at midspan of the 3D rotor are negligible, highlighting that 3D flow effects due to tip flows do not reach this position.

Examination of all profiles of Fig. 7(b) shows that the effects of blade finite-length effects are very small when the blade loading is low, i.e. when the angle of attack is low ($0° < \vartheta < 40°$and $130° < \vartheta < 210°$): in these portions of the revolution, the 2D and both 3D curves are almost superimposed. When the incidence increases, the blade load also increases and the blade starts experiencing stall. Figure 8 reports the top view of the vorticity contours at midspan at three azimuthal positions to examine the onset of stall in the upwind zone. At ϑ=70° a small separation region forms on the suction side of the blade. At ϑ=80° the blade stall has become significant, since the flow is detached from the blade. At the position of torque peak a large region of the suction surface is affected by stall. Consequently, the torque loss due to tip effects also increases because the strength of tip vortex flow increases with the flow incidence. The same behaviour can be seen also in the downwind zones. Closer inspection of the 2D and mean 3D CP curves shows that these effects are strongest in the upwind region of the period, where a maximum difference of 9.7 percent between the torque peaks occurs.

Examining the torque profiles at the spanwise positions considered in Fig. 4(a), some additional observations can be made:

- The torque profiles of the blade sections at 20%, 40% and 50% semispan are almost identical, indicating that at least half of the blade is characterized by a predominantly 2D flow with negligible impact of tip flow effects;
- The torque profiles of the blade sections at 60%, 70% and 80% show a progressive reduction of the torque peak, down to -14 percent with respect to the midspan section. The remainder of the torque curve is less affected, especially in the downwind zone;
- The torque profiles of the blade sections at 90%, 95% and 97.5% show that at these positions, 3D effects are strong throughout the whole revolution. Notably, in the regions of positive torque production, the efficiency is remarkably reduced;
- In proximity of the blade tip (99%), almost no positive contribution to the torque output is given, due to the large load reduction;
- The azimuthal position of the torque peak occurs later in the cycle as one moves towards the tip, with a 5° shift between the 0% and 97.5% sections. This can be explained with a reduction of the incidence angle (downwash), as shown below. The experiments of Li et al. [35] highlight the same trend and show that the aforementioned shift is even more pronounced for a turbine with a very low aspect ratio (AR=4.5).

To compare the CFD prediction of the impact of finite blade effects on turbine performance to that of the widespread low-fidelity BEM theory, Fig. 9 compares the 2D and mean 3D torque profiles obtained with NS CFD and the corresponding estimates obtained with the VARDAR research code, a state-of-the-art BEM code developed at the University of Florence [6,17-18] using the ubiquitous Leicester-Prandtl model for the finite-wing correction [58].The two BEM profiles of Fig. 9 differ in that one includes tip flow corrections and the other does not. Examination of these profiles shows that the reduction of the torque peak in the upwind portion of the revolution predicted by the CFD analyses is in good agreement with that estimated with the simplified tip flow model included in the BEM theory, and the shapes of the CFD and BEM torque profiles are in a qualitatively good agreement. Conversely, the patterns of the torque curves in the downwind portion of the revolution predicted by the BEM and CFD analyses are significantly different, and the torque reduction due to blade finite length predicted by the BEM analysis is higher than predicted by CFD. This comparative analysis highlights the potential of using CFD also for further improving the predictions of low-fidelity engineering tools, which are key to Darrieus rotor industrial design due to their extremely small computational requirements.

To provide a different quantitative perspective of the impact of tip losses, Fig. 10 compares the CFD and BEM profiles of mean torque coefficient per unit length. For each blade height the mean value is obtained by averaging the profiles of Fig. 4(a) over one revolution. The figure also reports the constant mean torque values of the 2D and 3D simulations for both the CFD and BEM models. All curves are normalized with respect to the mean 2D torque coefficient.One sees that the mean blade performance is almost unaffected by tip-effects up to approximately 70% semispan. More specifically, it is found that tip flow effects adversely affect the performance of the blade for a span length of approximately 2.6*c* (yellow zone in Fig. 10). In terms of aggregate data, the tip effects yield a reduction of the rotor torque of 8.6% with respect to the 2D calculation with virtually infinite span. This can be seen as an equivalent reduction of the actual blade's height of 0.75*c* for each half blade (red colored zone in Fig. 10). Such a correction factor needs to be accounted for when estimating the turbine performance by means of 2D simulations.

The observations above are in accordance with the findings of Li e al. [35] in terms of performance drop as a function of the distance from the tip. Their experiments showed that at 55% semispan, corresponding to a distance of 1.0*c* from the tip, the torque peak is greatly reduced. At this blade height, they found a *CP* reduction of 40% over the midspan value at TSR=2.2 and 60% at TSR=2.5, corresponding to an equivalent reduction of the actual blade's height by 1.8*c* and 2.7*c*, respectively. Other analyses focused on estimating the mean power reduction due to finite blade length effects through comparisons of 2D and 3D CFD analyses [32,33,37,40], but their results are not directly comparable with the present study due to the use of different aspect ratio, rotor solidity, TSR, airfoil geometry and number blades.. Overall, the equivalent height reduction can vary from 0.8*c* for a NACA 0022 three-blade rotor at TSR=1.3 [32] up to 5*c* for a NACA 0018 two-blade rotor at TSR=4.5 [33].

To investigate in greater detail the 3D phenomena accounting for energy efficiency reduction, the Mach contours and streamlines at the angular position of maximum separation (ϑ=120°) are examined in Fig. 11(a). Different spanwise sections are considered to analyse the flow pattern alterations from midspan to the blade tip.

In the central portion of the blade (from midspan to about 70% semispan) the streamlines are contained in planes orthogonal to the blade axis, indicating a predominantly 2D flow character, and a fairly large region of separated flow in the rear of the suction side. Closer to the tip (90% semispan) the downwash due to the tip flow reduces the effective AoA with respect to that at midspan, and the extension of the stall region is thus reduced. The skin friction lines and contours of the z velocity component (*w*) on the blade suction surface reported in Fig. 11(b) show the extension of the region affected by downwash. Near the tip, the flow on the pressure side is no longer able to follow the blade profile, and travels over the tip due to the pressure difference between the pressure side and the suction side. The tip vortex flow is responsible for the downwash velocity component and therefore for the incidence variation along the span, in accordance with the theory of finite wings [58]. It is noted that the finite wing effects occurring in Darrieus rotors are more complex than those encountered in fixed finite wings. This is primarily because of the flow curvature associated with the circular trajectory of the blade, and also the flow nonlinearities due to dynamic stall.

To quantify the impact of these effects, it is convenient to examine the curves of the torque coefficient per unit length at midspan and 90% semispan (Fig. 12). The percentage difference between the two curves (i.e. the torque coefficient difference between the curves at each azimuthal angle divided by the revolution-averaged torque coefficient at midspan) is also reported to quantify the dependence of the torque variation on the azimuthal position. A notable torque reduction occurs in the interval 40°<ϑ<130°. In addition, a large and sudden torque reduction occurs towards the end of the revolution, in the interval *315°*<ϑ<340°, a range in which the AoA is decreasing and goes below the value yielding stall. Also, an inversion in the expected trend is noticed close to ϑ=150°, where the tip section performs better than the midspan section: the torque of the section at 90% semispan is about 10 percent higher than that at midspan. According to the finite wing theory, the lift should be in fact always reduced in proximity of the tip. Therefore, the inversion at ϑ=150° cannot be explained with this theory alone. This occurrence and the sudden torque loss of the tip section towards the end of the revolution are analysed in further detail below.

To investigate the origin of the sudden torque reduction at the blade tip in the interval 315°<ϑ<340°, isosurfaces of the turbulent kinetic energy field at selected azimuthal positions are examined in Fig. 13. The color scale is based on the intensity of the velocity component along the z-axis (*w*). Three azimuthal positions of the blade are considered: ϑ=60°, ϑ=180° and ϑ=315°. During the upwind half of the revolution (ϑ=60°) the tip vortex is strong, since the vertical component of velocity is fairly high. A high turbulence region is then generated from the blade tip. At ϑ=180°, the region of high turbulent kinetic energy corresponding to the tip vortex is increased in size and length, and is still associated with large values of *w*. This strong vortex detaches from the blade, is convected by the wind, and is re-encountered by the blade at ϑ=315°. The blade interaction with this vortex induces a more pronounced reduction of the torque with respect to the 2D case, where this effect is absent.

To investigate the reasons for the higher torque of the 90% section over the midspan section at ϑ=150°, top views of the streamlines at ϑ=150° and ϑ=48° are examined in Fig. 14. The position ϑ=48° is selected because this is the other angular position of the upwind half of the revolution experiencing the same AoA of ϑ=150°. Streamlines on both the pressure and suction sides of the blade are visualized at four different span locations. At ϑ=48° the downwash effect is visible: moving from midspan to the tip, the incidence of the oncoming flow decreases and the air stream after the trailing edge is more aligned to the airfoil chord. This phenomenon is not very pronounced due to the low loading on the blade at this angular position. At ϑ=150°, moving from midspan to the tip, the incidence of the oncoming flow is progressively reduced similarly to what seen at ϑ=48°. However, the flow pattern on the suction side of the central portion of the blade is significantly different from that at ϑ=48°, despite the fact that the AoA is similar in the two cases. A large separation region exists at ϑ=150° due to stall. Due to the finite wing length, a strong modification of this flow pattern is observed moving towards the tip: from 70% semispan, the flow is attached due to lower downwash-induced loading and is more aligned to the airfoil chord after the trailing edge.

The observations above can be explained by a combined effect of downwash and dynamic stall. From ϑ=0° to ϑ=90° the AoA increases and stall in the central blade portion occurs between ϑ=70° and ϑ=80°. The dominant effect is that of the downwash which reduces the AoA to the outer portion of the blade. When the AoA reaches its maximum towards ϑ=90°, the central portion of the blade experiences high level of stall. From ϑ=90° to ϑ=180° the AoA decreases but the central portion of the blade remains stalled due to delay of the flow in readjusting to the decreasing incidence (a distinctive feature of dynamic stall). However, the outer sections of the blade remain stall-free, and this is the reason why at ϑ=150° the torque of the tip sections is higher than that of the midspan section, whereas the opposite is observed at ϑ=48°.

Fig. 15 presents an analysis of the same type of that of Fig. 14 for the angular positions ϑ=210° and ϑ=300°. Both positions belong to the downwind portion of the rotor trajectory and are characterized by a comparable AoA. However at ϑ=210° the AoA is increasing whereas at ϑ=300° the AoA is decreasing. One notices that the streamline pattern at ϑ=210° is similar to that at ϑ=48°. At ϑ=300° the streamline patterns from midspan to tip are the same as those at ϑ=210°. The similarity of the flow patterns at these two positions is due to the fact that no stall occurs in the downwind portion of the rotor trajectory.

Fig. 16 depicts the blade streamlines at ϑ=315°, the position at which the tip vortex interacts with the outboard portion of the blade in its downwind trajectory, as highlighted in Fig. 13. One observes a sudden deviation of the oncoming flow in the tip region with respect to the flow direction at midspan. Such deviation is due to the blade-vortex interaction, which prevails over the effects due to downwash.

All aforementioned results can be more quantitatively described by evaluating the pressure coefficient (C_p) distributions and the vorticity contours along the blade. The pressure coefficient used in this study is defined by Eq. (7), where p denotes the static pressure at the airfoil surface. Due to the difficulty of properly defining the actual relative wind speed at each blade height, the relative flow velocity w_{th} used to calculate C_p neglects the induced velocity and is computed using the vectorial sum of the absolute free-stream velocity and entrainment velocity ΩR.

Fig. 17 reports the C_p profiles at different blade heights for three key angular positions: maximum loading (ϑ=80°), inversion of torque of midspan and tip sections (ϑ=150°) and maximum loading in the downwind half of the revolution (ϑ=240°). The objective of this analysis is to highlight the impact of downwash and stall at different angular positions.

$$C_p = \frac{p - p_\infty}{\frac{1}{2}\rho_\infty w_{th}^2} \tag{7}$$

At ϑ=80° the blade is subject to high loading (high AoA and high relative speed). The top subplot of Fig. 17 confirms that, in these conditions, 3D flow effects affect almost 40 percent of the blade (from the tip to 60% semispan), since moving from midspan to the tip, the C_p profile at 60% already shows a slight loading reduction with respect to midspan. Closer to the tip, the suction side of the blade is characterized by an almost constant pressure, indicating that this blade portion generates a small lift. As a result, the torque of the tip sections is substantially lower than that of the midspan section, and the torque becomes negative at 97.5% midspan, as shown in Fig. 7. At ϑ=240° (middle subplot of Fig. 16) the AoA is high but the relative speed magnitude is lower than at ϑ=80°. In these conditions 3D flow effects affect only the last 20 percent of the semispan (i.e. from 80% semispan to tip): significant differences in the C_p profiles with respect to the midspan values are observed only on the last 10 percent of the blade, where the loading becomes significantly smaller than at midspan. Unlike at the two angular positions just discussed, a strong flow separation due to stall occurs at ϑ=150° (bottom subplot of Fig. 17). This is highlighted by the pressure profiles at 0% and 60% semispan, which feature a fairly shallow slope on the suction side. In this circumstance, the lower AoA at the tip sections induced by the tip vortex-related downwash results in the flow past such tip sections remaining attached and these sections outperforming the midspan region of the blade.

The evolution of the vorticity contours at different blade span heights is presented in Fig. 18. In the upwind half of the revolution, the two positions ϑ=40° and ϑ=140° are of particular interest. Although at these two positions the torque profiles along the blade are comparable (see Fig. 7(a) and Fig. 7(b)), the vorticity patterns and thus the flow field are remarkably different. On the other hand, moving to the downwind half of the revolution, one sees that the vorticity patterns around the blade are quite similar at all azimuthal positions. These patterns are in line with the previous analyses of streamlines and pressure coefficient profiles.

Figure 19 reports the top view of the vorticity contours at four different span locations at the two aforementioned azimuthal positions and highlights the vorticity differences in greater detail. At ϑ=40° the vorticity contours are very similar, moving from midspan to tip, whereas at ϑ=140° the large separation region due to stall is clearly visible along a large central portion of the blade.

4. Conclusions

A 3D time-accurate Reynolds-averaged Navier-Stokes CFD analysis of an aspect ratio 17.5 blade rotating in Darrieus-like motion has been presented. Special attention was paid to the description of 3D flow effects and their impact on the energy efficiency of Darrieus rotor blades. This was accomplished also by comparative analyses of 3D and 2D CFD analyses. The presented 3D CFD results were obtained with a highly refined analysis using a grid with 64 million elements and time-marching the flow field to a periodic state using 720 time-steps per revolution. A 3D mesh sensitivity analysis was also presented. The main outcomes of the analysis can be summarized as follows:

a) 3D flow effects due to finite blade length reduce the mean power of the considered 17.5 aspect ratio blade by 8.6 percent with respect to the torque of the corresponding infinite blade. Such mean torque reduction corresponds to a reduction of the effective blade length of 1.5c (0.75c for each half blade).
b) A strong interaction between the tip-vortex released in the upwind portion of the blade revolution and the blade traveling in the downwind region occurs at ϑ=315°, and this yields an additional reduction of the outboard blade sections in this region of the revolution.
c) Finite blade length effects do not modify significantly the overall shape of the blade torque profile over the revolution with respect to the torque profile of the corresponding infinite blade;
d) For given azimuthal position, the torque profile along the blade height varies substantially from midspan to tip, and the pattern of these variations strongly depends on the azimuthal position; i.e. on the magnitude of the relative velocity of the oncoming flow and its local angle of attack;
e) The mean torque reduction predicted by the 3D CFD analysis and that of a state-of-the-art BEM analysis using tip loss corrections is comparable, but the profiles of the blade torque in the downwind portion of the revolution differ significantly. The reliability of BEM analyses may be improved by using 3D CFD results to develop azimuthal position-dependent tip loss corrections;
f) The 3D grid sensitivity analysis highlighted that the use of a coarser grid, with size comparable to those used in most 3D Darrieus studies to date, may yield uncertainty levels in the prediction of tip vortex flows, blade/wake/tip vortex interactions, and dynamic stall timings and strength. All these phenomena affect torque and power generation. The mean power predicted by a typical coarse grid and the fine grid of this study differed by more than 3 percent. and significantly larger differences are expected for multi-blade rotors due to higher number of blade/wake/tip vortex encounters per revolution.

Future work will include investigating 3D flow effects at different tip-speed ratios, particularly the lower ones, at which the impact of dynamic stall is expected to be more pronounced than at the considered regime, and extending this analysis to multi-blade turbines, to assess in detail all aspects of wake/blade interactions. This type of high-fidelity analyses provides valuable data for validating and further improving the reliability of low-fidelity tools such as BEM codes and codes based on lifting line theory and free vortex transport methods. Due to their extremely high execution speeds, these engineering tools are of crucial importance to improving the design of future small and large Darrieus turbines.

Acknowledgements

We acknowledge use of Hartree Centre resources in this work. The STFC Hartree Centre is a research collaboratory in association with IBM providing High Performance Computing platforms funded by the UK's investment in e-Infrastructure. The Centre aims to develop and demonstrate next generation software, optimised to take advantage of the move towards exa-scale computing. Part of the reported simulations were also performed on two other clusters. One is POLARIS, part of the N8 HPC facilities provided and funded by the N8 consortium and EPSRC (Grant No.EP/K000225/1). The Centre is co-ordinated by the Universities of Leeds and Manchester. The other resource is the HEC cluster of Lancaster University, which is also kindly acknowledged. Finally, thanks are due to Prof. Ennio Antonio Carnevale of the Università degli Studi di Firenze for supporting this research.

References

[1] Paraschivoiu I. Wind turbine design with emphasis on Darrieus concept. Polytechnic International Press: Montreal (Canada), 2002.

[2] Darrieus GJM. Turbine having its rotating shaft transverse to the flow of the current. US Patent No.01835018, 1931.

[3] Tjiu W, Marnoto T, Mat S, Ruslan MH, Sopian K. Darrieus vertical axis wind turbine for power generation I: Assessment of Darrieus VAWT configurations. Renewable Energy 2015; 75(March 2015): 50-67. DOI: 10.1016/j.renene.2014.09.038

[4] Tjiu W, Marnoto T, Mat S, Ruslan MH, Sopian K. Darrieus vertical axis wind turbine for power generation II: Challenges in HAWT and the opportunity of multi-megawatt Darrieus VAWT development. Renewable Energy 2015; 75(March 2015):560-571. DOI: 10.1016/j.renene.2014.10.039

[5] Bianchini A, Ferrara G, Ferrari L. Design guidelines for H-Darrieus wind turbines: Optimization of the annual energy yield. Energy Conversion and Management 2015;89:690-707. DOI: 10.1016/j.enconman.2014.10.038

[6] Bianchini A, Ferrari L, Magnani S. Energy-yield-based optimization of an H-Darrieus wind turbine. Proceedings of the ASME Turbo Expo 2012, Copenhagen (Denmark), June 11-15, 2012. DOI: 10.1115/GT2012-69892

[7] Balduzzi F, Bianchini A, Carnevale EA, Ferrari L, Magnani S. Feasibility analysis of a Darrieus vertical-axis wind turbine installation in the rooftop of a building. Applied Energy 2012; 97: 921–929. DOI: 10.1016/j.apenergy.2011.12.008

[8] Mohamed MH. Aero-acoustics noise evaluation of H-rotor Darrieus wind turbines. Energy 2014; 65(1): 596-604. DOI: 10.1016/j.energy.2013.11.031.

[9] Bianchini A, Ferrara G, Ferrari L, Magnani S. An improved model for the performance estimation of an H-Darrieus wind turbine in skewed flow. Wind Engineering 2012; 36(6): 667-686. DOI: 10.1260/0309-524X.36.6.667

[10] Bausas MD, Danao LAM. The aerodynamics of a camber-bladed vertical axis wind turbine in unsteady wind. Energy 2015; 93: 1155-1164. DOI: 10.1016/j.energy.2015.09.120

[11] Danao LA, Edwards J, Eboibi O, Howell R. A numerical investigation into the influence of unsteady wind on the performance and aerodynamics of a vertical axis wind turbine. Applied Energy 2014; 116: 111-124. DOI: 10.1016/j.apenergy.2013.11.045

[12] Wekesa DW, Wang C, Wei Y, Zhu E. Experimental and numerical study of turbulence effect on aerodynamic performance of a small-scale vertical axis wind turbine. Journal of Wind Engineering and Industrial Aerodynamics 2016; 157: 1-14. DOI: 10.1016/j.jweia.2016.07.018

[13] Mertens S. Wind Energy in the Built Environment. Multi-Science: Brentwood (UK), 2006.

[14] Borg M, Collu M, Brennan FP. Offshore floating vertical axis wind turbines: advantages, disadvantages, and dynamics modelling state of the art. Marine & Offshore Renewable Energy Congress, London (UK), 26-27 September, 2012.

[15] Brahimi M, Allet A, Paraschivoiu I. Aerodynamic analysis models for vertical-axis wind turbines. International Journal of Rotating Machinery 1995; **2**(1): 15-21. DOI: 10.1155/S1023621X95000169

[16] Paraschivoiu I, Delclaux F. Double Multiple Streamtube Model with Recent Improvements. Journal of Energy 1983, 7(3), pp. 250-255.

[17] Bianchini A, Ferrari L, Carnevale EA. A model to account for the Virtual Camber Effect in the Performance Prediction of an H-Darrieus VAWT Using the Momentum Models. Wind Engineering 2011; 35(4): 465-482. DOI: 10.1260/0309-524X.35.4.465

[18] Marten D, Bianchini A, Pechlivanoglou G, Balduzzi F, Nayeri CN, Ferrara G, Paschereit CO, Ferrari L. Effects of airfoil's polar data in the stall region on the estimation of Darrieus wind turbines performance. J. of Engineering for Gas Turbines and Power 2016; 139(2): 022606-022606-9. DOI: 10.1115/1.4034326.

[19] Marten D, Lennie M, Pechlivanoglou G, Nayeri CD, Paschereit CO. Implementation, Optimization and Validation of a Nonlinear Lifting Line Free Vortex Wake Module within the Wind Turbine Simulation Code QBlade. Proc. of the ASME Turbo Expo 2015, Montréal, Canada, June 15-19, 2015.

[20] Deglaire P. Analytical Aerodynamic Simulation Tools for Vertical Axis Wind Turbines. Digital Comprehensive Summaries of Uppsala Dissertations from the Faculty of Science and Technology 2010, 704, ISSN 1651-6214.

[21] Amet E, Maitre T, Pellone C, Achard JL. 2D Numerical Simulations of Blade-Vortex Interaction in a Darrieus Turbine. Journal of Fluids Engineering 2009; 131: 111103.1–111103.15. DOI: 10.1115/1.4000258

[22] Simao-Ferreira C, van Zuijlen A, Bijl H, van Bussel G, van Kuik G. Simulating dynamic stall on a two-dimensional vertical-axis wind turbine: verification and validation with particle image velocimetry data. Wind Energy 2010; 13: 1-17. DOI: 10.1002/we.330

[23] Salvadore F, Bernardini M, Botti M. GPU accelerated flow solver for direct numerical simulation of turbulent flows. Journal of Computational Physics 2013; 235: 129-142. DOI: 10.1016/j.jcp.2012.10.012

[24] Raciti Castelli M, Englaro A, Benini E. The Darrieus wind turbine: Proposal for a new performance prediction model based on CFD. Energy 2011; 36: 4919-4934. DOI: 10.1016/j.energy.2011.05.036

[25] Balduzzi F, Bianchini A, Maleci R, Ferrara G, Ferrari L. Critical issues in the CFD simulation of Darrieus wind turbines. Renewable Energy 2016; 85(01): 419-435. DOI: 10.1016/j.renene.2015.06.048

[26] Bianchini A, Balduzzi F, Ferrara G, Ferrari L. Aerodynamics of Darrieus Wind Turbines Airfoils: The Impact of Pitching Moment. J. Eng. Gas Turbines Power 2016;139(4):042602-042602-12. DOI:10.1115/1.4034940

[27] Rainbird J, Bianchini A, Balduzzi F, Peiro J, Graham JMR, Ferrara G, Ferrari L. On the Influence of Virtual Camber Effect on Airfoil Polars for Use in Simulations of Darrieus Wind Turbines. Energy Conversion and Management 2015;106:373-384. DOI: 10.1016/j.enconman.2015.09.053

[28] Bianchini A, Balduzzi F, Ferrara G, Ferrari L. Virtual incidence effect on rotating airfoils in Darrieus wind turbines. Energy Conversion and Management 2016;111(1 March 2016):329-338. DOI: 10.1016/j.enconman.2015.12.056

[29] Bausasa MD, Danao LAM. The aerodynamics of a camber-bladed vertical axis wind turbine in unsteady wind. Energy 2015;93(Part 1, 15 December 2015):1155–1164. DOI: 10.1016/j.energy.2015.09.120

[30] Asra MT, Nezhad EZ, Mustapha F, Surjatin Wiriadidjajac. Study on start-up characteristics of H-Darrieus vertical axis wind turbines comprising NACA 4-digit series blade airfoils. Energy 2016;112(1 October 2016):528–537. DOI: 10.1016/j.energy.2016.06.059

[31] Zuo W, Wang X, Kang S. Numerical simulations on the wake effect of H-type vertical axis wind turbines. Energy 2016;104(1 June 2016):295–307. DOI: 10.1016/j.energy.2016.02.127

[32] Howell R, Qin N, Edwards J, Durrani N. Wind tunnel and numerical study of a small vertical axis wind turbine. Renewable Energy 2010; 35: 412-422. DOI: 10.1016/j.renene.2009.07.025

[33] Lam HF, Peng HY. Study of wake characteristics of a vertical axis wind turbine by two- and three-dimensional computational fluid dynamics simulations. Renewable Energy 2016; 90(May 2016): 386-398. DOI: 10.1016/j.renene.2016.01.011

[34] Yakhot V, Orszag SA, Thangam S, Gatski TB, Speziale CG. Development of turbulence models for shear flows by a double expansion technique. Physics of Fluids 1992;4(7):1510-1525.

[35] Li Q, Maeda T, Kamada Y, Murata J, Kawabata T, Shimizu K, Ogasawara T, Nakai A, Kasuya T. Wind tunnel and numerical study of a straight-bladed vertical axis wind turbine in three-dimensional analysis (Part I: For predicting aerodynamic loads and performance). Energy 2016; 106(1 July 2016):443–452. DOI: 10.1016/j.energy.2016.03.089

[36] Menter FR. Two-equation Turbulence-models for Engineering Applications. AIAA Journal 1994; 32(8): 1598-1605. DOI: 10.2514/3.12149

[37] Gosselin R, Dumas G, Boudreau M. Parametric study of H-Darrieus vertical-axis turbines using uRANS simulations. Proc. of the 21st Annual Conference of the CFD Society of Canada, May 6-9, Sherbrooke (Canada), 2013

[38] Joo S, Choi H, Lee J. Aerodynamic characteristics of two-bladed H-Darrieus at various solidities and rotating speeds. Energy 2015;90(Part 1 - October 2015):439–451. DOI: 10.1016/j.energy.2015.07.051

[39] Li Q, Maeda T, Kamada Y, Murata J, Kawabata T, Shimizu K, Ogasawara T, Nakai A, Kasuya T. Wind tunnel and numerical study of a straight-bladed Vertical Axis Wind

Turbine in three-dimensional analysis (Part II: For predicting flow field and performance). Energy 2016; 104(1 June 2016):295-307. DOI: 10.1016/j.energy.2016.03.129

[40] Alaimo A, Esposito A, Messineo A, Orlando C, Tumino D. 3D CFD Analysis of a Vertical Axis Wind Turbine. Energies 2015; 8: 3013-3033. DOI: 10.3390/en8043013

[41] De Marco A, Coiro DP, Cucco D, Nicolosi F. A Numerical Study on a Vertical-Axis Wind Turbine with Inclined Arms. International Journal of Aerospace Engineering 2014; 2014: 1-14. DOI: 10.1155/2014/180498

[42] Zamani M, Nazari S, Moshizi SA, Maghrebi MJ. Three dimensional simulation of J-shaped Darrieus vertical axis wind turbine. Energy 2016;116(Part 1 - 1 December 2016):1243–1255. DOI: 10.1016/j.energy.2016.10.031

[43] Orlandi A, Collu M, Zanforlin S, Shires A. 3D URANS analysis of a vertical axis wind turbine in skewed flows. Journal of Wind Engineering and Industrial Aerodynamics 2015; 147(December 2015): 77-84. DOI: 10.1016/j.jweia.2015.09.010

[44] Elkhoury M, Kiwata T, Aoun E. Experimental and numerical investigation of a three-dimensional vertical-axis wind turbine with variable-pitch. J. Wind Eng. Ind. Aerodyn. 2015;139:111–123. DOI: 10.1016/j.jweia.2015.01.004

[45] Balduzzi F, Bianchini A, Ferrara G, Ferrari L. Dimensionless numbers for the assessment of mesh and timestep requirements in CFD simulations of Darrieus wind turbines. Energy 2016;97(15 February 2016):246-261. DOI: 10.1016/j.energy.2015.12.111

[46] Almohammadi KM, Ingham DB, Ma L, Pourkashan M. Computational fluid dynamics (CFD) mesh independency techniques for a straight blade vertical axis wind turbine. Energy 2013; 58(1 September 2013): 483-493. DOI: 10.1016/j.energy.2013.06.012

[47] Daróczy L, Janiga G, Petrasch K, Webner M, Thévenin D. Comparative analysis of turbulence models for the aerodynamic simulation of H-Darrieus rotors. Energy 2015; 90(1 October 2015): 680-690. DOI: 10.1016/j.energy.2015.07.102

[48] Campobasso MS, Piskopakis A, Drofelnik J, Jackson A. Turbulent Navier-Stokes Analysis of an Oscillating Wing in a Power Extraction Regime Using the Shear Stress Transport Turbulence Model. Computers and Fluids 2013; 88: 136-155. DOI: 10.1016/j.compfluid.2013.08.016

[49] Drofelnik J and Campobasso MS, Comparative Turbulent Three-Dimensional Navier-Stokes Hydrodynamic Analysis and Performance Assessment of Oscillating Wings for Renewable Energy Applications, International Journal of Marine Energy, Vol. 16, 2016, pp. 100-115

[50] Campobasso MS, Gigante F, Drofelnik J. Turbulent Unsteady Flow Analysis of Horizontal Axis Wind Turbine Airfoil Aerodynamics Based on the Harmonic Balance Reynolds-Averaged Navier-Stokes Equations. ASME paper GT2014-25559, Proc. of the ASME Turbo Expo 2014, Düsseldorf (Germany), 2014. DOI:10.1115/GT2014-25559.

[51] Campobasso MS, Drofelnik J, Gigante F, Comparative Assessment of the Harmonic Balance Navier-Stokes Technology for Horizontal and Vertical Axis Wind Turbine Aerodynamics, Computers and Fluids, Vol. 136, 2016, pp. 354-370.

[52] Campobasso MS, Baba-Ahmadi MH. Analysis of Unsteady Flows Past Horizontal Axis Wind Turbine Airfoils Based on Harmonic Balance Compressible Navier-Stokes

Equations with Low-Speed Preconditioning. ASME Journal of Turbomachinery 2012; 134(6): 061020-1-13. DOI: 10.1115/1.4006293.

[53] Balduzzi F, Bianchini A, Gigante FA, Ferrara G, Campobasso MS, Ferrari L. Parametric and Comparative Assessment of Navier-Stokes CFD Methodologies for Darrieus Wind Turbine Performance Analysis. Proc. of the ASME Turbo Expo 2015, Montreal, Canada, June 15-19, 2015. DOI: 10.1115/GT2015-42663

[54] Dossena V, Persico G, Paradiso B, Battisti L, Dell'Anna S, Brighenti A, Benini E. An Experimental Study of the Aerodynamics and Performance of a Vertical Axis Wind Turbine in a Confined and Non-Confined Environment. Proc. of the ASME Turbo Expo 2015, Montreal, Canada, June 15-19, 2015

[55] Jameson A, Baker TJ. Solution of the Euler equations for complex configurations. AIAA paper 83-1929, July 1983. 6th AIAA computational fluid dynamics conference, Danvers, Massachusetts.

[56] Balduzzi, F., Bianchini, A., Marten, D., Drofelnik, J., Pechlivanoglou, G., Nayeri, C.N., Ferrara, G., Paschereit, C.O., Campobasso M.S. and Ferrari, L., 2017, "Three-dimensional aerodynamic analysis of a Darrieus wind turbine blade using computational fluid dynamics and lifting line theory", Proc. of the ASME Turbo Expo 2017, Charlotte, USA, June 26-30, 2017

[57] http://community.hartree.stfc.ac.uk/wiki/site/admin/resources.html, last accessed 10/05/2016.

[58] Abbott IH, Von Doenhoff AE. Theory of Wing Sections. New York, USA: Dover Publications Inc.; 1959.

FIGURES

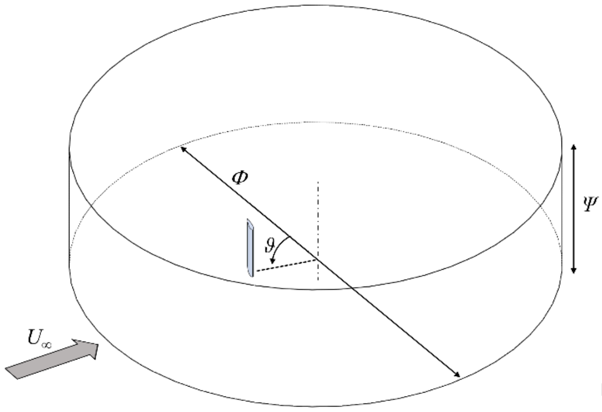

Figure 1 - Computational domain.

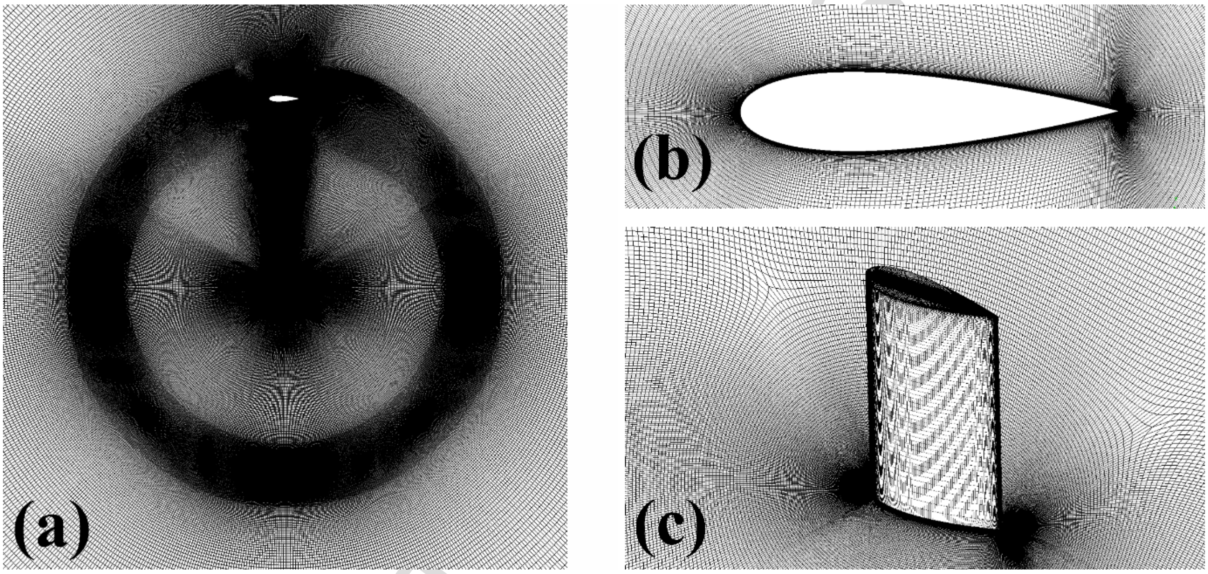

Figure 2 - Some details of the computational mesh.

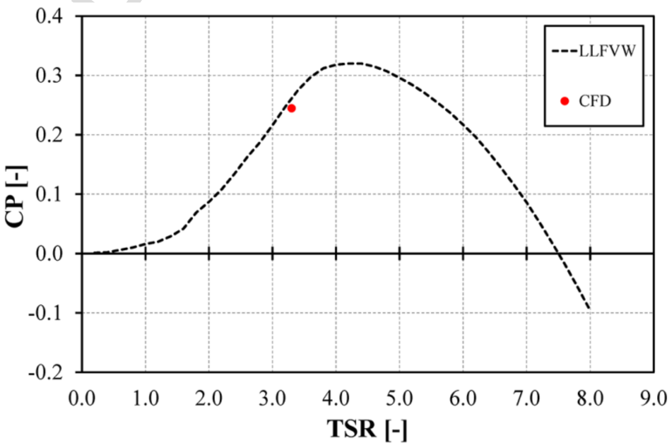

Figure 3 - Attended power curve of the 1-blade model.

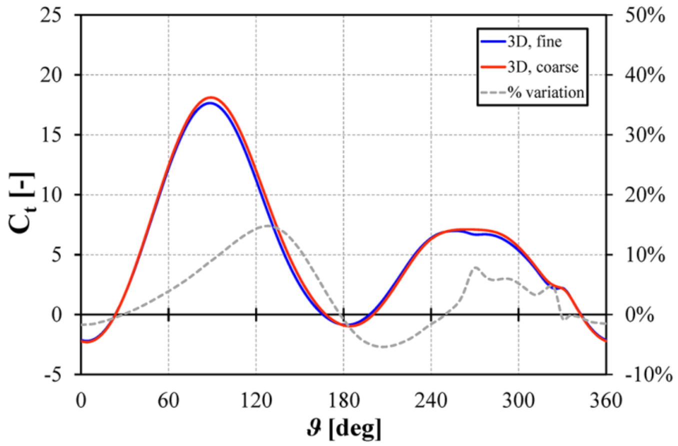

Figure 4 - Differences in the torque profile between the selected mesh and a coarser one.

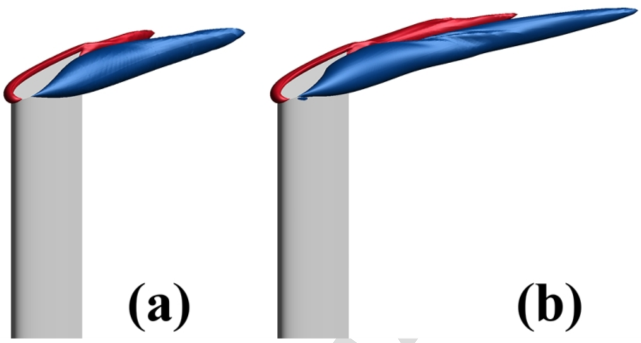

Figure 5 – Tip vortices generated at ϑ=80°: (a) coarse mesh; (b) selected mesh.

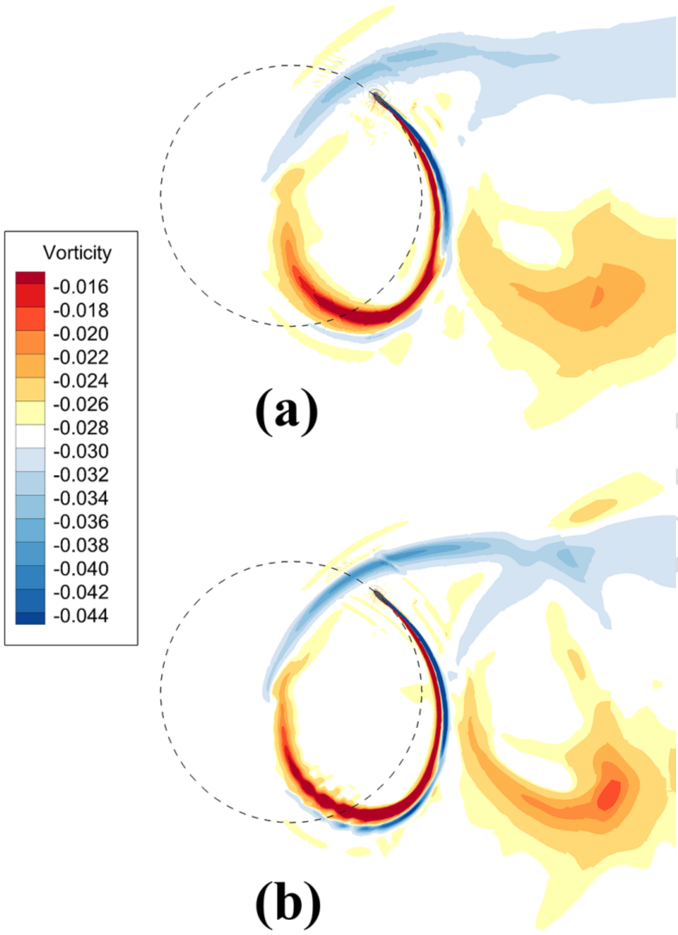

Figure 6 - Vorticity contours at midspan at ϑ=315°: (a) coarse mesh; (b) selected mesh.

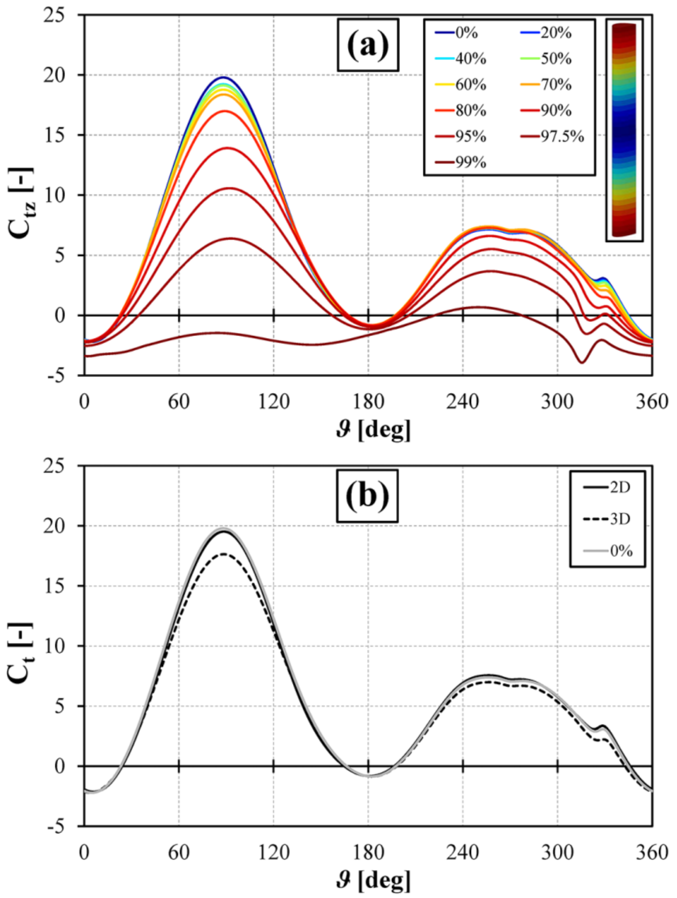

Figure 7 - Torque coefficient vs azimuthal angle: (a) variation at different span lengths; (b) 2D simulations compared to the 3D profile at midspan and average 3D profile.

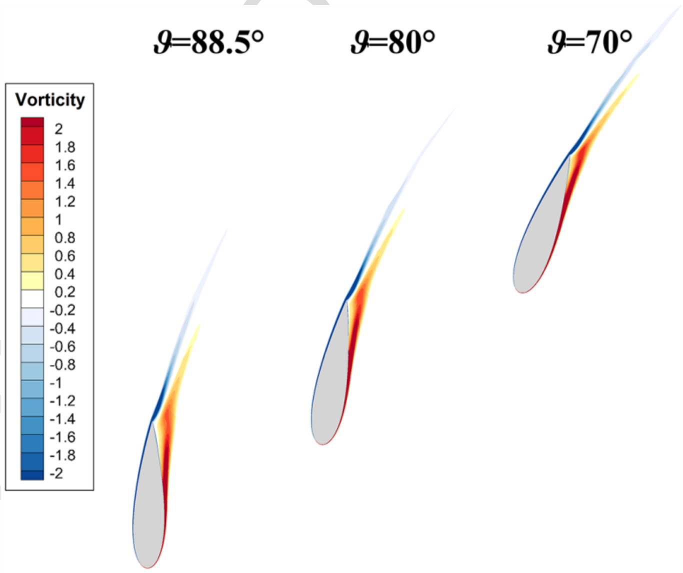

Figure 8 - Vorticity contours at midspan: ϑ=70°, ϑ=80° and ϑ=88.5°.

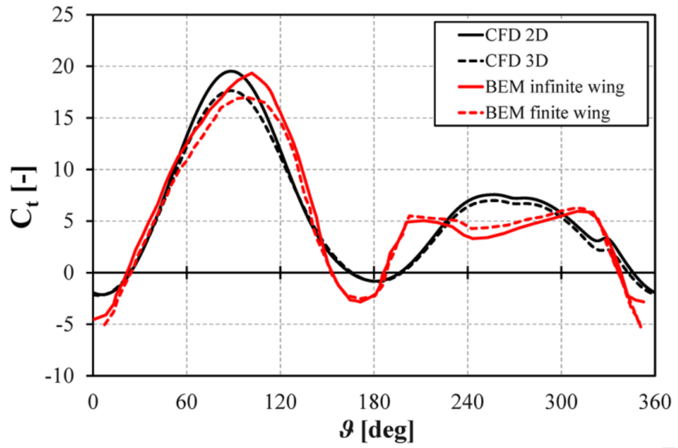

Figure 9 - Torque coefficient profiles: 2D and 3D CFD data vs. BEM simulations either including or neglecting the finite-wind effects.

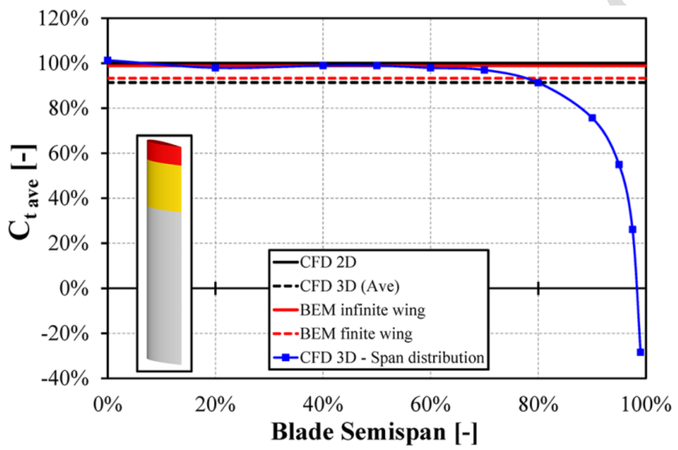

Figure 10 - Torque coefficient distribution along the semispan.

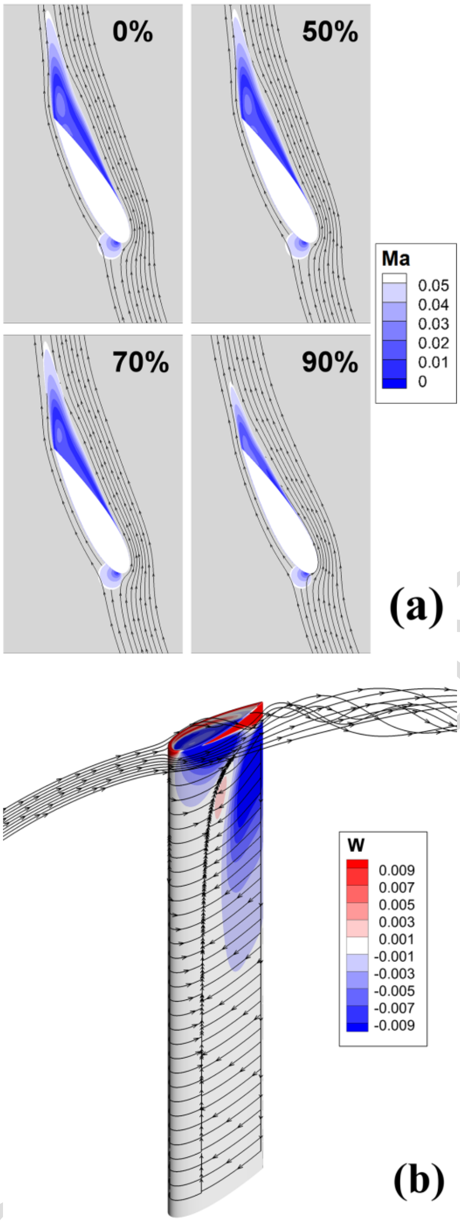

Figure 11 – Downwash effect at ϑ=120°: (a) Mach contours and streamlines at different semispan locations; (b) flow streamlines in the tip region, skin friction lines and z velocity component on the blade suction surface.

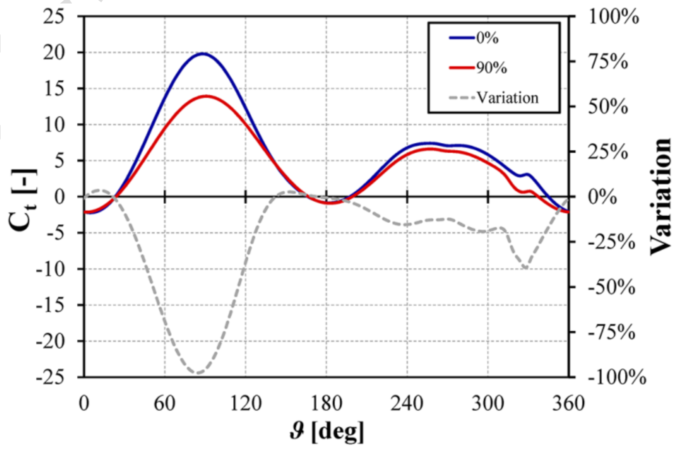

Figure 12 - Comparison of torque coefficient curves at 0 and 90 percent semispan.

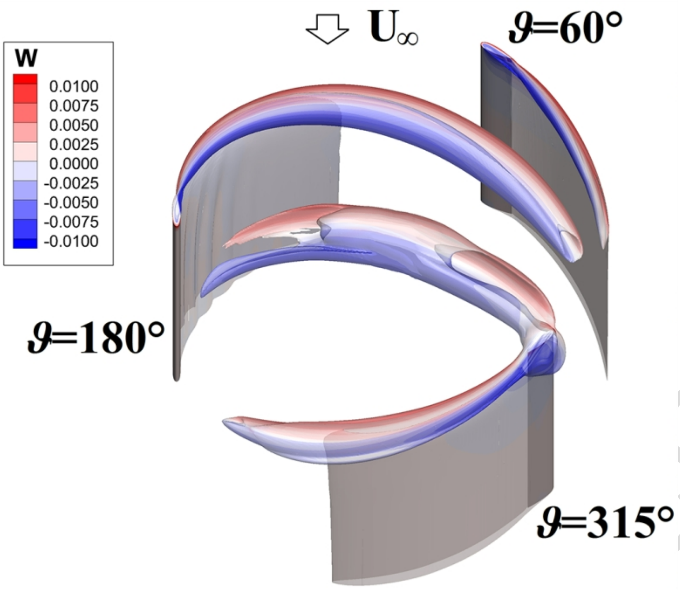

Figure 13 - Isosurfaces of turbulent kinetic energy *k* colored with the contour of *w*.

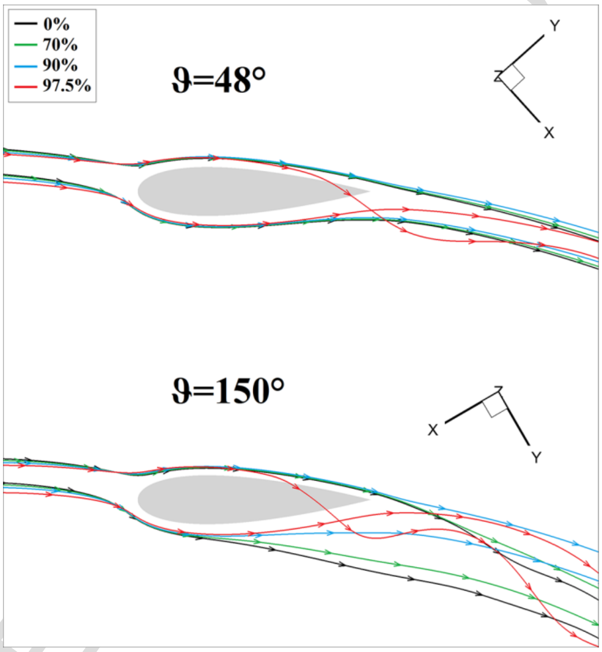

Figure 14- Streamlines at different span lengths: ϑ=48° and ϑ=150°.

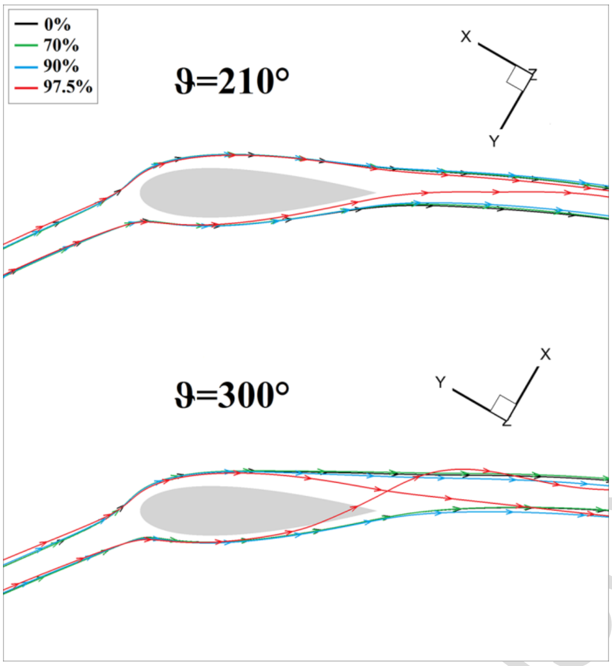

Figure 15 - Streamlines at different span lengths: ϑ=210° and ϑ=300°.

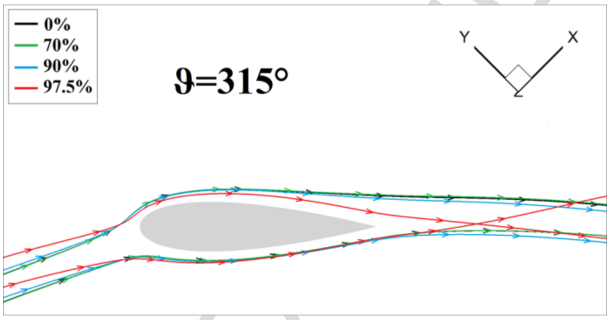

Figure 16 - Streamlines at different span lengths: ϑ=315°.

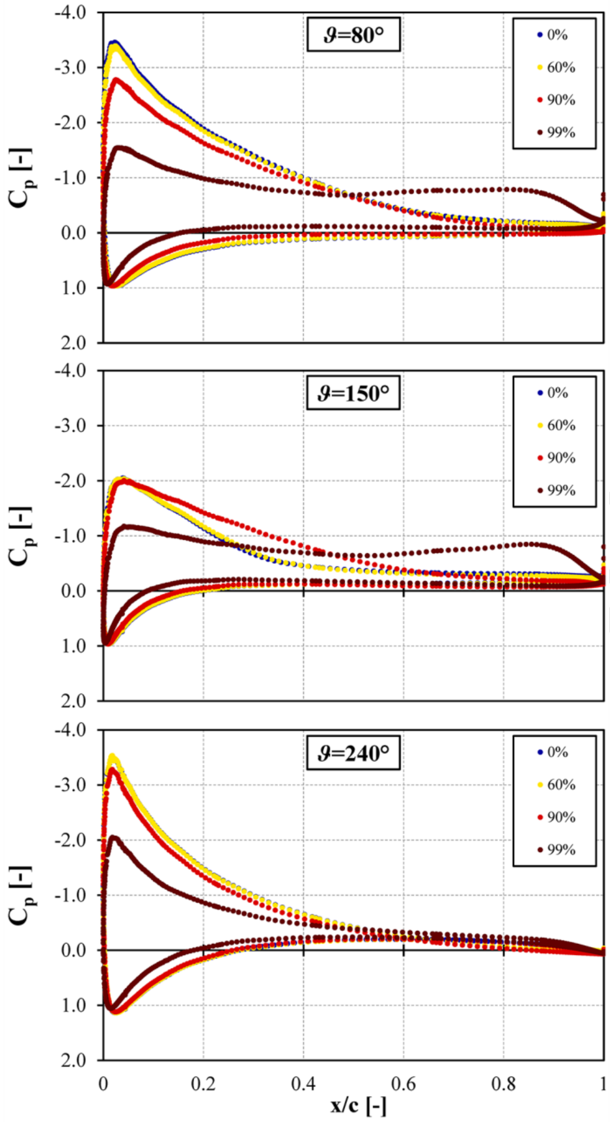

Figure 17 - Pressure coefficient profiles at different span lengths: ϑ=80°, ϑ=150° and ϑ=240°.

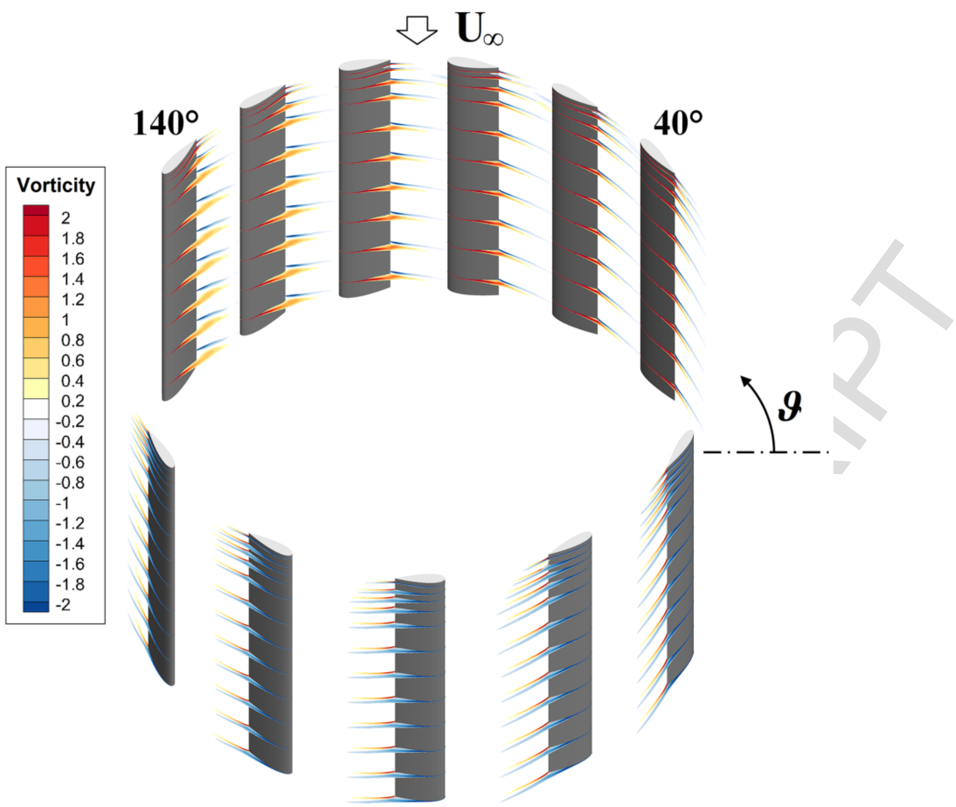

Figure 18 - Vorticity contours at different span lengths during the revolution.

963

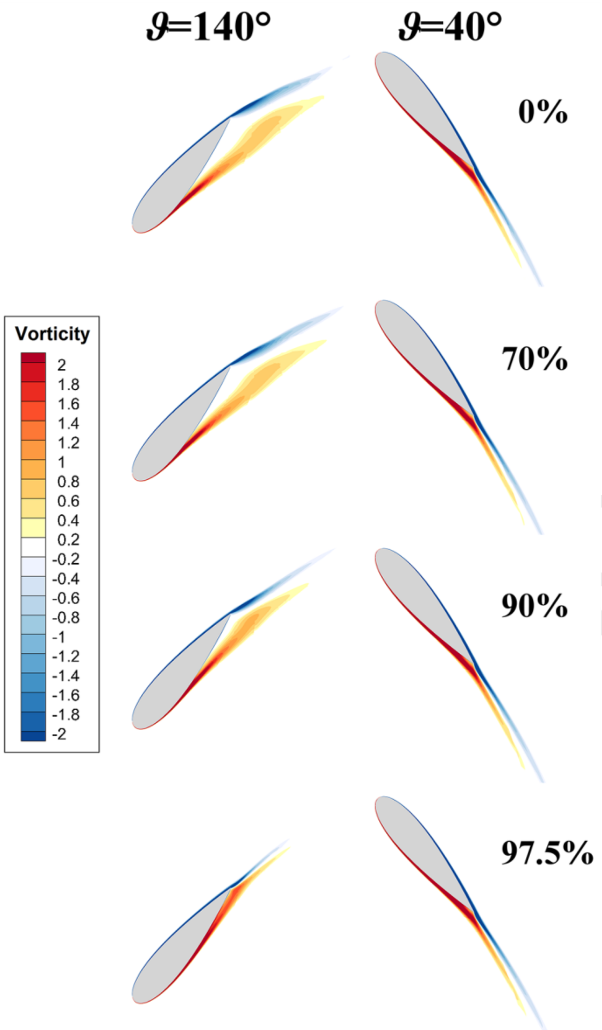

964 **Figure 19 - Vorticity contours at different semispan locations: ϑ=40° and ϑ=140°.**